This is the author's version of an article that has been published in this journal. Changes were made to this version by the publisher prior to publication.
The final version of record is available at http://dx.doi.org/10.1109/JSEN.2017.2774705

A Wideband, Low-noise Accelerometer for Sonar Wave Detection

F. Edalatfar, S. Azimi, A.Q. Ahsan Qureshi, B. Yaghootkar, A. Keast, W. Friedrich, A. Leung, and B. Bahreyni, *Senior Member, IEEE*

***Abstract*—This paper presents the development of a high-performance micromachined capacitive accelerometer for detection of sonar waves. The device is intended to replace existing hydrophones in towed array sonar systems, and thus, needs to meet stringent performance requirements on noise, bandwidth, and dynamic range, among others. The in-plane, single-axis accelerometer is designed based on a mode-tuning structural platform. A frame was used instead of a solid plate for the proof-mass of the device, allowing us to push undesired vibration modes beyond the operating bandwidth of the device while enabling us to employ a portion of the area for capacitive sensing elements. The designed accelerometer was fabricated on a silicon-on-insulator wafer with 100µm device layer with capacitive gaps of ~2.2µm. The sensitivity of the accelerometer is 4.0V/g with a noise spectral density of better than $350\mathrm{ng}/\sqrt{\mathrm{Hz}}$. The fundamental resonant frequency of the device is 4.4kHz. The open loop dynamic range of the accelerometer, while operating at atmospheric pressure, is better than 135dB with a cross-axis sensitivity of less than 30dB.**

***Index Terms*—Accelerometer, Capacitive, Sonar wave detection, Low-noise, Wide-bandwidth, Micro-electromechanical systems.**

I. INTRODUCTION

The term *sonar* refers to the methods and equipment for detecting, locating, and determining the nature of underwater objects using acoustic waves [1]. Sonar wave detection is a fundamental requirement in many applications, including seabed mapping, oil and gas exploration, pipeline inspections, marine life research, underwater threat detection, and search and rescue missions. Passive sonar systems silently listen to acoustic signals generated by various sources in the environment. Active sonar systems, on the other hand, emit acoustic signals and then listen for echoes in addition to the potential signals generated by objects. The principal sensors used for sonar detection are hydrophones, omnidirectional transducers which measure the local strength of an incoming acoustic pressure wave. A towed array is a sonar system that employs a large number of hydrophones in order to locate the source of emitted or reflected acoustic signals. A towed array is made by arranging hydrophones as sensing nodes along a linear array at regular intervals within an elastomeric hose that is deployed behind a vessel underneath the sea surface. The acoustic signal arriving from a distant source reaches each hydrophone within the array at a slightly different time. Using the Time Difference of Arrival (TDoA) method, the location of the source can be determined [2]. However, there is a left-right ambiguity in the recognition of the source location due to the inverse trigonometric function operations (i.e., there are two mirrored, valid solutions for the location of the signal source on either side of the towed array). To resolve this ambiguity, each single hydrophone at each node is replaced with four hydrophones which are placed at the corners of a square. The time difference between the signals received by the four hydrophones is used to determine the orientation of the signal. The diameter of the circular array needs to be a significant fraction of the wavelength [3]. Otherwise, the difference-output signal between the hydrophones in a single node will be too small to resolve the ambiguity issue. A typical towed array cable is about 10cm in diameter and can be several hundred meters long. As the towed array needs to stay buoyant, such a system can weigh several tons [4]. The volume, weight, speed, and minimum achievable radius of the towed array put stringent requirements on the winch that deploys or retrieves the array. Consequently, a major portion of the cost of towed array systems is spent on the winch that can meet the size, power, and speed requirements for the application. Additionally, the size and power requirements for the winches are only met by the larger naval vessels. To use the towed array systems on smaller ships, it is required to significantly reduce the diameter of the array.

An alternative method for detecting the acoustic waves is to utilize neutrally buoyant particle acceleration sensors; i.e. accelerometers. Unlike hydrophones, the output of an accelerometer is proportional to both amplitude and direction of their input signal. A neutrally buoyant object that is small compared to the acoustic wavelength has similar acceleration characteristics to the acoustic wave [5]. According to Newton's second law applied to fluid particles, the pressure gradient (∇p) in a fluid with density ρ_0 is proportional to the fluid's particles acceleration (a) through $\nabla\vec{p} = -\rho_0\vec{a}$ [3]. Therefore, a single 2-axis particle acceleration sensor, or two

Submitted on August 1, 2017. This work was supported in part by the Natural Sciences and Engineering Research Council of Canada (NSERC).
F. Edalatfar, S. Azimi, A.Q.A. Qureshi, B. Yaghootkar, and B. Bahreyni are with the School of Mechatronic Systems Engineering at Simon Fraser University, Surrey, BC, V3T 0A3 Canada.
A. Keast and W. Friedrich are with Ultra-Electronics Maritime Systems, Dartmouth, NS, B2Y 4N2 Canada.
A. Leung is with the School of Engineering Sciences at Simon Fraser University, Burnaby, BC, V5A 1S6 Canada.
Corresponding author is Behraad Bahreyni (behraad@ieee.org).

Copyright (c) 2017 IEEE. Personal use is permitted. For any other purposes, permission must be obtained from the IEEE by emailing pubs-permissions@ieee.org.

This is the author's version of an article that has been published in this journal. Changes were made to this version by the publisher prior to publication.
The final version of record is available at http://dx.doi.org/10.1109/JSEN.2017.2774705

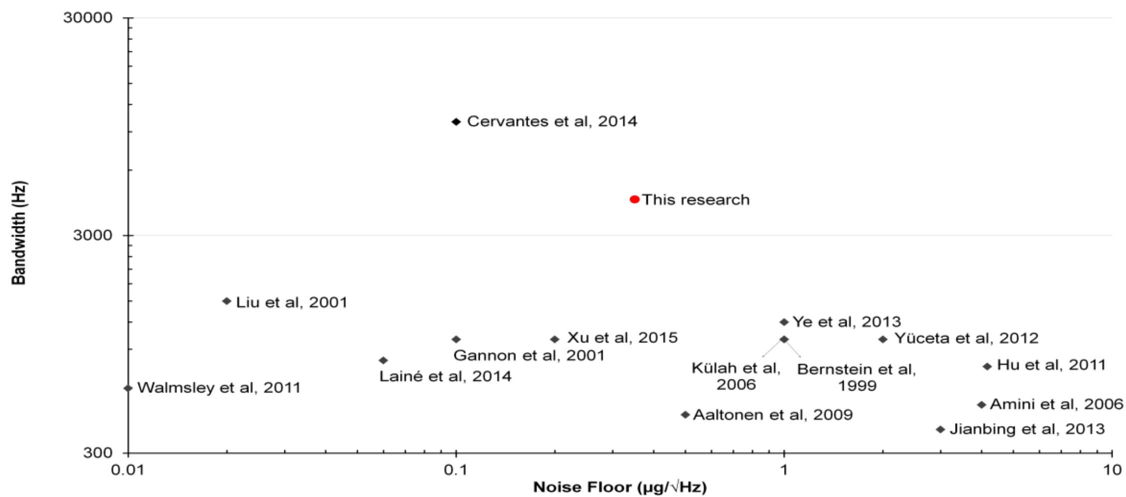

Fig. 1. Comparison of micro-accelerometers based on reported performance of bandwidth and noise floor [10], [11], [15]–[27].

stacked single-axis accelerometers, can substitute the quad hydrophone module at each node. Upon this substitution, the diameter of the carrier hose in the towed array could be decreased down to the diameter of a single micromachined accelerometer. However, detection of sonar waves places rather challenging requirements on the performance of accelerometers. The noise floor of the accelerometer should be less than $0.5\mu g/\sqrt{Hz}$ to be able to operate down to quiet ocean ambient levels, where g is the acceleration due to earth's gravity ($1g \approx 9.81 m/s^2$) [6]. The dynamic range of the accelerometer should be more than 140dB (within a 1-Hz bandwidth) to enable it to listen to weak echoes while the ship transmitter is operating. The accelerometer needs to cover a fairly wide frequency range, typically between 50Hz and 4.2kHz plus DC. The combination of these requirements present a multitude of challenges and trade-offs for the design of accelerometers that can be used for sonar applications.

Several high-performance accelerometers have been developed for various applications over the past few decades, with the majority trading noise performance with bandwidth [7]–[9]. Liu et al. developed an electron tunneling accelerometer aimed at the underwater acoustics applications [10]. This accelerometer operated at a pressure of about 1 Pa to achieve a noise level of $20ng/\sqrt{Hz}$. The mechanical bandwidth of the system was increased from its resonance frequency of 100Hz to above 1kHz using a feedback controller. This device, however, required a complicated manufacturing process and a sophisticated controller for the highly nonlinear tunneling transduction. Laine et al. developed a capacitive low noise accelerometer with an 800Hz closed-loop bandwidth [11]. This accelerometer has a reported noise level of $10ng/\sqrt{Hz}$ at 70Hz with a dynamic range of 130dB. This accelerometer is commercialized as part of a land seismic acquisition system [12]. Gannon et al. developed a capacitive analog servo accelerometer [13], [14]. The reported noise level of the accelerometer is $100\,ng/\sqrt{Hz}$ at 200Hz with bandwidth and dynamic range of 200Hz and 115dB, respectively. Walmsley et al. developed a two axis, in-plane capacitive MEMS accelerometer [15]. The noise level of the accelerometer was measured to be $10ng/\sqrt{Hz}$ at full bandwidth of 200Hz with a dynamic range of 120dB. A wide bandwidth along with sub-$\mu g/\sqrt{Hz}$ noise floor was reported for an opto-mechanical accelerometer which was developed by Cervantes et al. [16]. This optical accelerometer is a combination of a mechanical fused-silica oscillator and fiber-optic micro-mirror cavities. The noise floor of this device was reported to be $100ng/\sqrt{Hz}$ for the frequencies between 1.5kHz and 10kHz. However, because of the complex packaging and interface requirements, optical accelerometers are not still viable candidates for most applications.

Fig. 1 compares the high-performance accelerometers reported in the literature in terms of their noise and bandwidth specifications. Despite the ongoing interest and efforts in this field, there is no high-performance accelerometer that can meet all the requirements for sonar wave detection. This paper is a study to develop a single axis capacitive in-plane accelerometer with sub-µg noise floor, wide bandwidth, and high dynamic range for sonar wave detection.

II. Device Design

The two main design criteria for the accelerometer system in this research were noise level of less than $0.5\mu g/\sqrt{Hz}$ and bandwidth of better than 4.2kHz. In this section, first, the two major challenges in designing low noise, wide bandwidth capacitive accelerometers are explained. Afterward, the mode-tuning platform to address these challenges is elaborated [28].

A single axis accelerometer can be modelled by a second order mass-damper-spring system. The fundamental resonance frequency (ω_0) of the accelerometer system for vibrations in the sense direction is:

$$\omega_0 = \sqrt{\frac{K_{eff}}{M_{eff}}} \quad (1)$$

where K_{eff} and M_{eff} are the effective stiffness and mass of the mechanical structure in the sense direction, respectively.

At frequencies far below the resonance frequency, the displacement of the proof-mass (Δy) is given by:

$$\Delta y = \frac{M_{eff}\, a_{in}}{K_{eff}} = \frac{a_{in}}{{\omega_0}^2} \quad (2)$$

Copyright (c) 2017 IEEE. Personal use is permitted. For any other purposes, permission must be obtained from the IEEE by emailing pubs-permissions@ieee.org.

This is the author's version of an article that has been published in this journal. Changes were made to this version by the publisher prior to publication.
The final version of record is available at http://dx.doi.org/10.1109/JSEN.2017.2774705

where a_{in} is the applied acceleration along the sense axis. As evident from Equation (2), the low-frequency proof-mass displacements are quadratically proportional to the inverse of the resonance frequency, presenting a challenge in measurement of displacements for devices with high resonant frequencies. Even though some sensing techniques employ structures beyond their resonance frequencies, in most cases, the mechanical resonance frequency is considered to be the upper limit for the operating frequency of a system due to the rapid decline of signal at higher frequencies. Taking DC to fundamental resonance frequency as the operating bandwidth of the sensor, Equation (2) demonstrates the explicit inverse relationship between the proof-mass displacements and the square of the desired operating bandwidth. To be able to measure exceedingly small proof-mass displacements, one needs to improve the rate of capacitance change per displacement of proof-mass. Using an interface circuit that measures the absolute changes in capacitance, decreasing the sensing gap or increasing the area between the sensing electrodes will improve the overall sensitivity of the system.

The lower limit for the capacitive sensing gap is typically dictated by the achievable aspect ratio in the etching process. The capacitive sensing area can be increased by employing a larger number of fingers in a comb structure, which can lead to an increase in device's surface area. Design with a proof-mass with a large surface to thickness ratio would entail undesired out-of-plane vibration modes, including asymmetric modes, into the working bandwidth of the device. The combination of inter-related phenomena described in the above remain main challenges in designing high-performance, wide-bandwidth accelerometers.

Another challenge in designing high performance accelerometers is meeting the low-noise requirements. If the noise sources are uncorrelated, the total noise equivalent acceleration (TNEA) of the accelerometer system is due to the mechanical noise equivalent acceleration (MNEA) and electrical noise equivalent acceleration (ENEA):

$$\mathrm{TNEA} = \sqrt{\mathrm{MNEA}^2 + \mathrm{ENEA}^2} \qquad \left[\frac{\mathrm{m}/_{s^2}}{\sqrt{\mathrm{Hz}}}\right] \tag{3}$$

ENEA is essentially produced by the electronic components. The MNEA is found from [29]:

$$MNEA = \sqrt{\frac{4k_B T \omega_{0,y}}{Q\ M_{eff}}} \tag{4}$$

where k_B is Boltzmann constant, T is the operating temperature in Kelvin, and Q is quality factor of the system. The MNEA can be practically reduced by increasing the effective mass of the moving structure (M_{eff}) or increasing the quality factor (Q). For most micromachined structures, viscous damping is the dominant loss mechanism. Quality factor can thus be increased by placing the device under vacuum. In addition to the cost and challenges of maintaining a stable level of vacuum within the package, increasing the Q presents practical challenges such as out-of-band excitation, ringing, and difficulty in feedback control. On the other hand, a large proof-mass necessitates a large surface area for the device due to the limitations in the thickness of the structural layers for MEMS devices. Such a plate with a small thickness to length ratio can have unwanted flexural modes within the desired operational bandwidth of the device.

To address the aforementioned challenges, the proof-mass structure was modified to push the undesired resonant modes past the operating bandwidth of the device. In order to suppress the unwanted flexural modes, elastic elements and anchor points were placed within the plate that constitutes the proof-mass of a device. We also populated a portion of the internal area of the proof-mass with comb-fingers to improve the device sensitivity. These modifications essentially converted the proof-mass from a solid body to a moving frame. The location of anchors and sensing elements was determined through an iterative process aimed at suppressing unwanted mode shapes. It is noteworthy that addition of each mode suppression element changes the dynamic response of the structure. Additional elements were added to the best existing modified structure as needed.

Fig. 2 shows the schematic design of the proposed accelerometer with modified proof-mass structure, illustrating the moving frame for the proof-mass, suspension beams, anchor points. The sensing axis of the accelerometer is along the *y*-direction. As shown in Fig. 2, the accelerometer has twelve elastic elements: six within the frame and six around it. These elements together provide the needed stiffness for the first mode, while collectively act to suppress undesired the flexural vibration modes. Using finite element models in

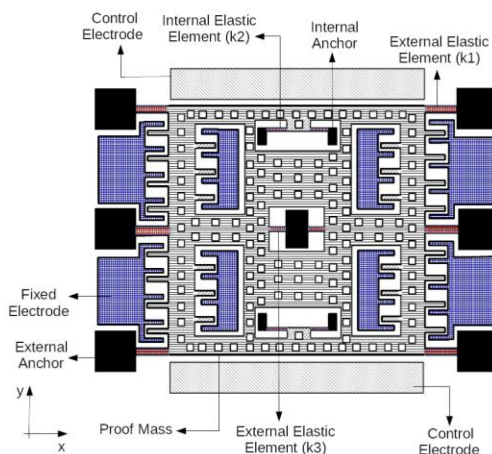

Fig. 2. Top view of the designed accelerometer.

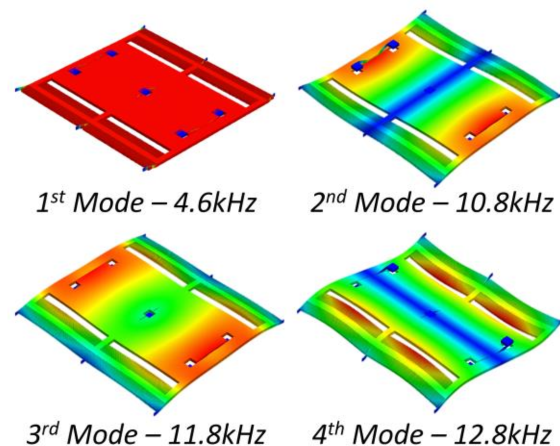

Fig. 3. The first four resonance frequencies of the accelerometer.

Copyright (c) 2017 IEEE. Personal use is permitted. For any other purposes, permission must be obtained from the IEEE by emailing pubs-permissions@ieee.org.

This is the author's version of an article that has been published in this journal. Changes were made to this version by the publisher prior to publication.
The final version of record is available at http://dx.doi.org/10.1109/JSEN.2017.2774705

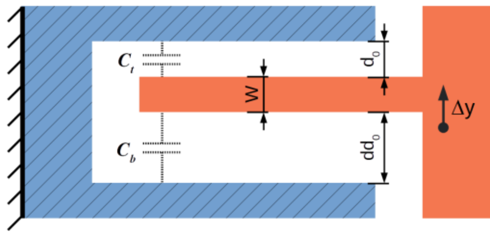

Fig. 4. Asymmetric interdigitated capacitive comb fingers.

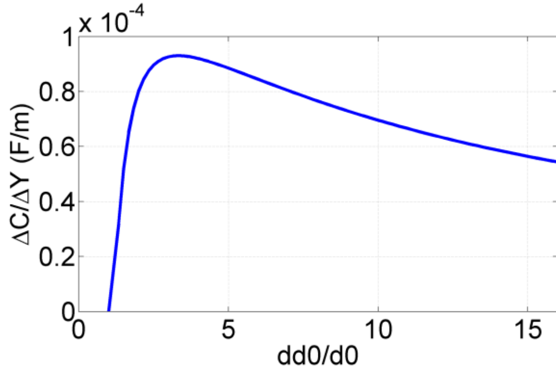

Fig. 5. Change in total capacitance as a function of the ratio of the gaps on the two sides of each finger.

CoventorWare™, mode shapes and frequencies for the accelerometer were obtained. The dynamic analysis of the accelerometer shows that the first resonance frequency of the accelerometer corresponds to an in-plane vibration mode with a frequency of 4.6kHz. Fig. 3 shows the first four mode shapes of the accelerometer. The second mode is away from the first mode by more than 6kHz.

After designing the mechanical structure of the accelerometer, the sensing electrodes, which are the capacitive comb structures, were optimized. In transverse capacitive comb configuration, the combs on the proof-mass move relative to the combs which is fixed to the substrate. As shown in Fig. 4, with only one routing layer available, each moving comb finger is located between two stationary fingers with different gaps, d_0, and dd_0, forming 2 parallel capacitors, C_t and C_b. As the proof-mass moves, the changes in capacitances of these two capacitors oppose each other. The total capacitance changes are dominated by the variations in the smaller gap. In order to decrease the adverse effect of the large gap on the capacitance change, it is desirable to increase the larger gap as much as possible. However, this would entail an inefficient use of the possible chip area. Hence, in order to achieve maximum sensitivity, a compromise should be established between the number of comb fingers (n) and the dd_0/d_0 ratio. The relation between changes in capacitance value (ΔC), small gap value (d_0), finger width (W), and gap ratio ($\alpha = \frac{dd_0}{d_0}$) is:

$$\Delta C = n\frac{2\varepsilon\,\Delta y A({d_0}^2-(\alpha d_0)^2)}{({d_0}^2-\Delta y^2)((\alpha d_0)^2-\Delta y^2)} = \frac{L}{2\omega + d0(1+\alpha)}\cdot\frac{2\varepsilon\,\Delta y A(1-\alpha^2)}{{d_0}^2\left(1-\left(\frac{\Delta y}{d_0}\right)^2\right)\left(\alpha^2-\left(\frac{\Delta y}{d_0}\right)^2\right)} \quad (5)$$

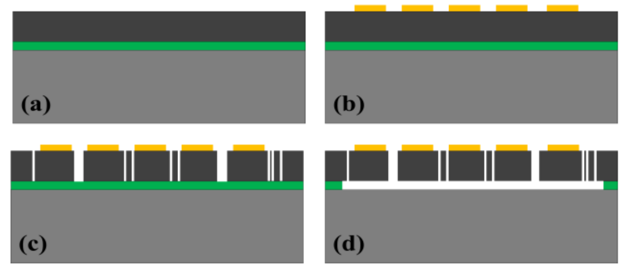

Fig. 6. Fabrication Process of the accelerometer, a) Starting substrate is an SOI wafer with 100μm device layer, 5μm buried oxide (BOX) layer, and 500μm handle wafer, b) Metal deposition using lift-off, c) Device layer patterning with DRIE, and d) Release using vapor HF.

where Δy is the relative displacement of the fingers from their initial position which is equal to the proof-mass displacement.

Taking into account the maximum achievable aspect ratio, i.e., the thickness of the structural layer over the minimum achievable gap between electrodes, an optimized value for α can be obtained. Fig. 5 demonstrates the achievable capacitance change rates for the targeted dimensions of the accelerometer and the minimum achievable gap in our fabrication process (~2.2μm). As seen, a ratio of $\alpha = \frac{dd_0}{d_0} \approx 3$ maximizes the change in capacitance for a given displacement of the proof-mass.

III. Fabrication Process

The accelerometer was bulk micro-machined on Silicon-On-Insulator (SOI) wafer. A P-type (100) SOI wafer with 0.01Ω-cm resistivity was used as the starting material, comprising a 100μm device layer, a 5μm buried oxide (BOX) layer, and a 500μm handle layer. Fig. 6 summarizes the fabrication process of the accelerometer. The process comprised a three masks process which included 2 lithography steps and a shadow mask. The shadow mask was used to deposit coarse gold mounting areas on the backside of the wafer as needed for the packaging step. Lithography was performed to define the metal contact pads. Following that, 20nm of chromium and 200nm of gold were deposited on the device layer of the SOI wafer using physical vapor deposition and lift-off process. In the next step, a 2.2μm layer of silicon dioxide was deposited on the device layer using plasma enhanced chemical vapor deposition (PECVD). This layer was used as a hard mask for Deep Reactive Ion Etching (DRIE). After patterning the hard mask in a Reactive Ion Etching (RIE) process, the device layer of the wafer was etched by DRIE. The wafer was diced using Stealth Laser Dicing technology [30]. Finally, the chips were released by etching the buried oxide (BOX) layer using vapor hydrofluoric (HF) acid, which also removed the PECVD oxide from the top surface and electrodes. The released devices were then individually packaged in leadless ceramic chip carriers using gold-tin solder as the adhesive between the gold layer on the backside of the chips and the package. The die attach process was performed in a reflow vacuum oven. The packaged devices were wire bonded using a semi-automatic wire bonder. It is possible to control the pressure inside the package using gold-tin sealing rings to solder a lid to the package, if desired. The devices reported in this paper were tested under atmospheric pressure. Fig. 7 shows a cross-

Copyright (c) 2017 IEEE. Personal use is permitted. For any other purposes, permission must be obtained from the IEEE by emailing pubs-permissions@ieee.org.

This is the author's version of an article that has been published in this journal. Changes were made to this version by the publisher prior to publication.
The final version of record is available at http://dx.doi.org/10.1109/JSEN.2017.2774705

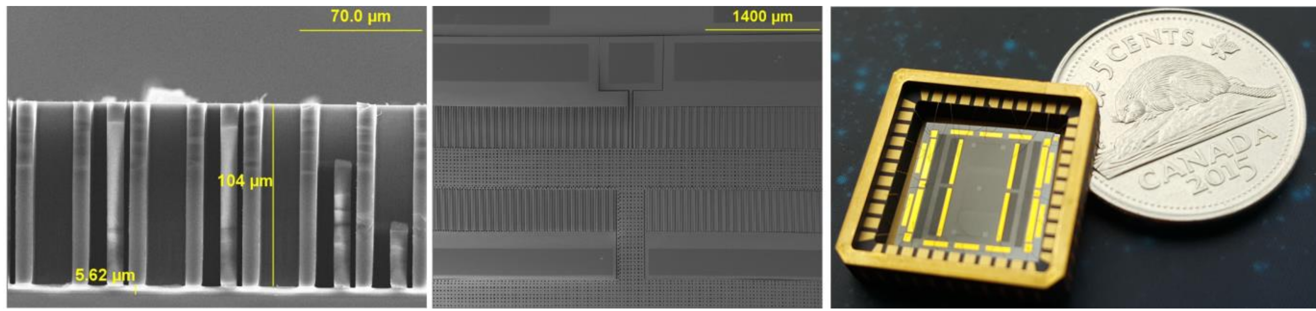

Fig. 7. Cross section of the fingers (left); Top view of the electrodes and moving frame (middle); and Packaged accelerometer (right).

section of etched structures, a top-view of the accelerometer, and a packaged accelerometer. The elastic beam elements, anchors, etch holes, and the electrodes can be clearly observed. The DRIE process could achieve a depth to gap ratio of 100µm:2.2µm.

IV. Interface Electronics

In order to convert the capacitive changes of the accelerometer to a voltage, a transimpedance amplifier (TIA) combined with a synchronous demodulator is used as the interface circuit. Synchronous demodulation helps to extract the small output signal of the accelerometer by providing excellent control over the noise bandwidth and performing the signal amplification at frequencies above the $1/f$ noise corner of typical amplifiers. Fig. 8 shows the simplified block diagram of the readout circuit. Two sense combs are driven by sinusoidal signals with 180º phase difference and the output signal is read through the proof-mass. The proof-mass potential is held at virtual ground by the TIA. The accelerometer's output current goes through the feedback resistor (R_f) and is converted to a voltage at the output of the TIA. The amplitude of this voltage is proportional to the capacitance changes of the accelerometer (ΔC) in the flat-band region of the amplifier:

$$V_1 = 4\pi f_d \, R_f \, \Delta C \, |V_d| \cos\left(2\pi f_d t + \varphi\right) \quad (6)$$

where f_d and $|V_d|$ are the frequency and amplitude of the drive signal and φ is its phase difference with the drive signal due to the speed limitations of the TIA and parasitics. The TIA's output signal is then applied to a synchronous demodulator. The output voltage of the demodulator circuit is:

$$V_2 = 1/2 \, |V_1||V_r| \left[\cos(4\pi f_d t + \varphi + \varphi') + \cos(\varphi - \varphi')\right] \quad (7)$$

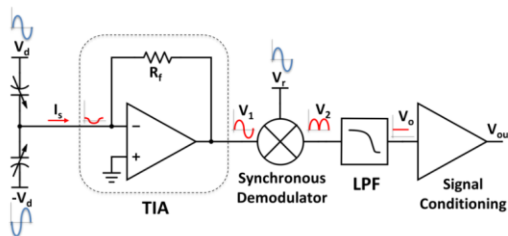

Fig. 8. Simplified block diagram of the readout circuit.

where $|V_r|$ is the amplitude of the synchronous demodulator reference signal and φ' is its phase difference with the drive signal. The low-pass filter removes the high frequency components outside of the bandwidth of the sensor. Knowing

$$|V_1| = 4\pi f_d |V_d| R_f \Delta C \quad (8)$$

and adjusting the reference signal to be in-phase with the TIA output ($\varphi = \varphi'$), the amplitude of the final output signal is:

$$|V_o| = 2\pi f_d |V_d||V_r| R_f \Delta C \quad (9)$$

The OPA656 FET-input operational amplifier from Texas Instruments was used for the transimpedance amplifier with an R_f value of 100kΩ. The AD835 analog multiplier from Analog Devices was used as the demodulator. The drive voltage frequency is set to 1MHz with maximum amplitude of 4.5V. The sensitivity of the circuit is ~4.0V/pF. Considering that he sensitivity of the mechanical system is ~1pF/g, the overall sensitivity of the accelerometer system is ~4.0V/g.

V. Experimental Results

Two sets of experiments, as described below, were conducted on packaged accelerometers. The first set of experiments was conducted in order to verify the basic performance metrics of the accelerometer using the typical research tools within our laboratory. The second set of experiments was conducted at our partner's underwater test facilities. These tests included frequency response specification and cross axis sensitivity performance analysis.

A. *Laboratory Experiments*

These experiments included frequency response specification, quality factor estimation, linearity analysis, and noise performance analysis. To study the frequency response of the sensor, it was tested on a high-frequency shaker while the vibration frequency was varied from 50Hz to 6kHz. However, due to the large size and structural discontinuities of the fixture and board, numerous resonance peaks were observed. In order to resolve this issue and eliminate contributions of the fixture and circuit board to the measured output of the sensor, the devices were tested electrostatically. The control electrodes above and below the proof-mass (see Fig. 2) were used to apply an electrostatic force to the proof-mass whose displacements were measured using the comb fingers. Using the test setup shown in Fig. 9, the proof-mass was biased with a DC voltage of 1V and actuated with a 50mV AC signal applied differentially to the control electrodes whose

Copyright (c) 2017 IEEE. Personal use is permitted. For any other purposes, permission must be obtained from the IEEE by emailing pubs-permissions@ieee.org.

This is the author's version of an article that has been published in this journal. Changes were made to this version by the publisher prior to publication.
The final version of record is available at http://dx.doi.org/10.1109/JSEN.2017.2774705

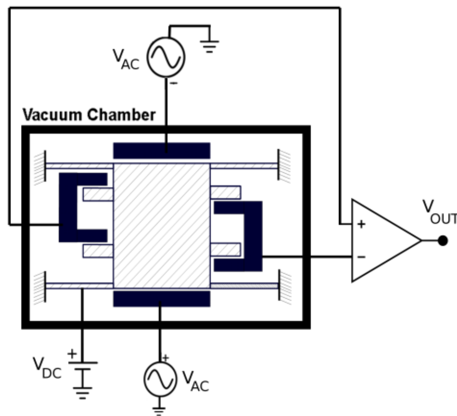

Fig. 9. Frequency response test setup using electrostatic actuation.

frequency was swept from 50Hz to 6kHz. The applied electrostatic force would correspond to ~1mg input acceleration signal.

The quality factor of the fundamental resonant mode was less than 1 at atmospheric pressures. As such, the resonant peak of the device was supressed. An experiment was performed using setup shown in Fig. 9 to evaluate the achievable quality factor values for the device. In this experiment, the frequency responses of the accelerometer under various pressures were recorded. Once a strong resonance peak was observed, the quality factor of the accelerometer was calculated at that pressure. As shown in Fig. 10, the quality factor is inversely related to the ambient pressure. Fig. 11 shows the resonance characteristics of the accelerometer at a pressure of about 20Pa. The high quality factor pushes the resonance peak well above the background signal. The resonance frequency of the accelerometer was then measured to be 4.4kHz which is in good agreement with the

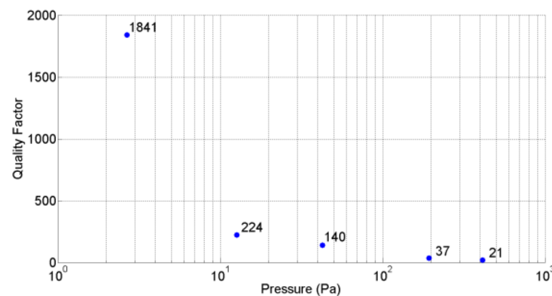

Fig. 10. Changes in quality factor as a function of ambient pressure, indicating viscous damping remains the main source of energy loss down to pressures as low as few pascals.

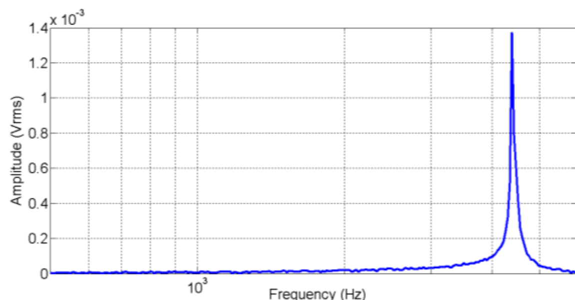

Fig. 11. Measured frequency response of the accelerometer at a pressure of 20Pa.

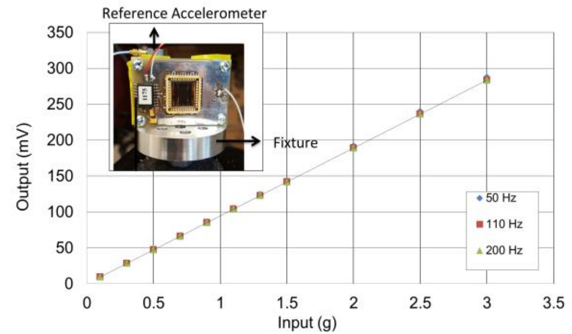

Fig. 12. Linearity test of the accelerometer, $R^2 = 0.99$.

simulated frequency of 4.6kHz.

In order to evaluate the linearity of the accelerometer system, the device was mounted on a fixture threaded to an electromagnetic shaker with its sensitive axis along the shaker excitation axis. For this test, the accelerometer was subjected to accelerations from 0.1g to 3g at 50Hz, 110Hz, and 200Hz frequencies. The results are shown in Fig. 12. The maximum applied acceleration to the device was 3g, limited by the shaker used. As it is evident from Fig. 12, there is no significant nonlinearity for input signals up to 3g. Based on this experiment, the nonlinearity of the device in the range of experiment was less than 0.7%.

Evaluating the noise performance of the accelerometer system was a significant part of this research. Mechanical Noise Equivalent Acceleration (MNEA) is found from equation (4). The Electrical Noise Equivalent Acceleration (ENEA) is dominated by the TIA noise at the drive frequency and can be estimated from:

$$ENEA = \left[\frac{v_{ne}}{G_s}\right] \tag{10}$$

where v_{ne} in $V/\sqrt{Hz}$ is the spectral density of the voltage noise of the readout circuit and G_s (V/g) is the system total gain. Circuit simulation predicted an output noise floor of 1µV/√Hz in the flat-band region of the readout circuit corresponding to ENEA of 0.25µg/√H z.

In order to verify the simulated results, output signal of the circuit was captured using National Instruments PXI-4462, a 24-bit, 204.8kS/s dynamic signal analyzer. The captured data was processed in MATLAB® and the spectral density of the TNEA was extracted [31]. Fig. 13 shows the measured TNEA of the complete system in frequency domain. The observed

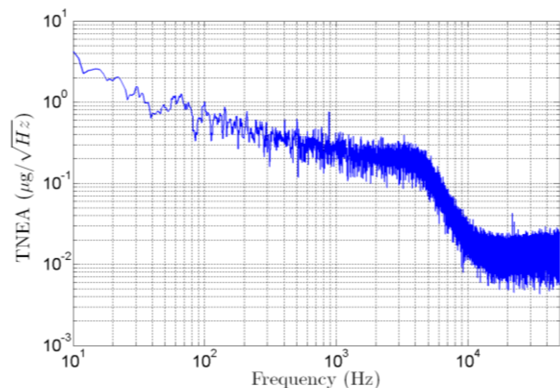

Fig. 13. Measured TNEA of the accelerometer.

Copyright (c) 2017 IEEE. Personal use is permitted. For any other purposes, permission must be obtained from the IEEE by emailing pubs-permissions@ieee.org.

This is the author's version of an article that has been published in this journal. Changes were made to this version by the publisher prior to publication.
The final version of record is available at http://dx.doi.org/10.1109/JSEN.2017.2774705

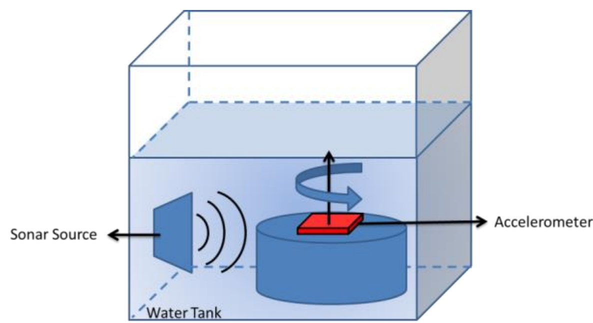

Fig. 14. Test setup for measuring the cross-axis sensitivity of the accelerometer using sonar waves.

$1/f$ noise at frequencies below 1kHz is most likely from the active circuits that follow the demodulator (i.e., the low-pass filter and signal conditioning stage in Fig. 8). The total sensor noise between 1kHz and 5kHz is in good agreement with our simulation results. The low-pass filter attenuates the output noise at frequencies above 5kHz until it reaches the minimum noise floor of the measurement setup at around 10kHz.

The dynamic range of the sensor, defined as the ratio of the largest to the smallest measurable signals, is calculated to be better than 135dB in a 1Hz bandwidth. The smallest detectable signal was taken to be equal to total noise of the sensor (i.e., signal to noise ratio of 1). The largest signal we could apply to the device was about 3g, limited by our shaker's performance.

B. Underwater experiments

In this set of experiments, directional performance and frequency response of the accelerometer were evaluated in the underwater facilities using sonar signals.

In order to analyze the cross-axis sensitivity of the device, the accelerometer and its interface circuit were sealed and placed inside a pressure vessel which was acoustically matched to water. The system was placed inside a vibration-isolated pool at our partner's testing facilities. The module was left powered and submerged in the tank overnight to ensure a stable operating temperature. The test setup is shown in Fig. 14. The pulsed sonar source was emitting sound waves at 3kHz. At the receiving end, the accelerometer assembly was rotated with a constant angular rate while the output of the accelerometer was recorded. Fig. 15 illustrates the magnitude

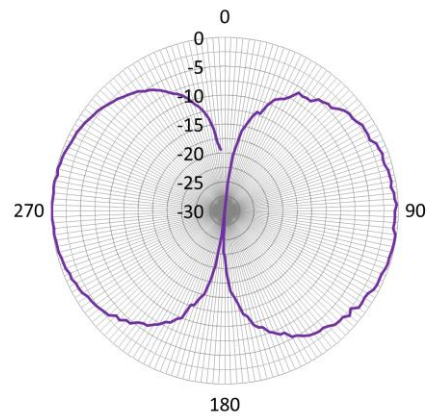

Fig. 15. Cross-axis sensitivity of the accelerometers measured using sonar waves.

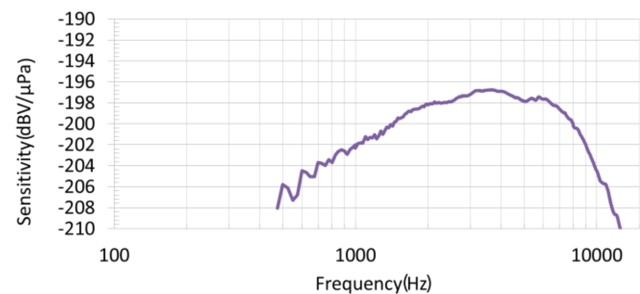

Fig. 16. Frequency response of the developed accelerometer to sonar waves of varying frequency.

of the sensor output versus the deviation angle from the sonar source on a polar plot, where at 0º, the accelerometer sense axis is perpendicular to the acoustic source emission axis. As can be seen, the cross-axis sensitivity of the accelerometer exhibits nulls of better than 30dB along the directions normal to the desired axis of sensitivity. Using the setup shown in Fig. 14 at a fixed angle, the dynamic response of the accelerometer was also measured. In this test, the pulsed sonar source generated signals from 500Hz to 11kHz, and the output of the accelerometer was recorded. The result is shown in Fig. 16.

A summary of the measured performance metrics for the developed accelerometer system is shown in Table 1. This data was used in Fig. 1 to provide a context for this work in relative to previously reported.

TABLE I
DEVICE SPECIFICATIONS AND PERFORMANCE SUMMARY

MEMS Device	
Active Die area	8mm×8mm
Brownian noise floor	200 $\mathrm{ng}/\sqrt{\mathrm{Hz}}$
Resonance frequency	4.4 kHz
Sensitivity	1 pF/g
Rest capacitance	202 pF
Cross axis sensitivity	< -30 dB
MEMS Device + Interface Circuit	
Dynamic range	$>$ 130dB (1Hz BW)
Noise floor	< 350 $\mathrm{ng}/\sqrt{\mathrm{Hz}}$
Overall sensitivity	4.0 V/g
Nonlinearity	< 0.7 %

CONCLUSIONS

This paper reported on the development and characterization of a high-performance micromachined accelerometer that can be used for the detection of sonar signals. We presented a method to increase the operating bandwidth of micromachined accelerometers while maintaining a high sensitivity and low-noise. The proof-mass of the accelerometer was a moving frame that provided a large area for sensing electrodes whose undesired vibration modes were suppressed by placement of anchors and elastic elements within and around it. The developed accelerometer could achieve a noise level of less than $350\,\mathrm{ng}/\sqrt{\mathrm{Hz}}$ while maintaining a wide bandwidth of 4.4kHz. The stiffness of the structure allowed for achieving a dynamic range of better than 135dB. To the best of our knowledge, this combination of high performance metrics is unprecedented for micromachined accelerometers.

Copyright (c) 2017 IEEE. Personal use is permitted. For any other purposes, permission must be obtained from the IEEE by emailing pubs-permissions@ieee.org.

This is the author's version of an article that has been published in this journal. Changes were made to this version by the publisher prior to publication.
The final version of record is available at http://dx.doi.org/10.1109/JSEN.2017.2774705

ACKNOWLEDGMENTS

This project was supported by Ultra Electronics Maritime Systems Inc. and Natural Sciences and Engineering Research Council of Canada (NSERC). Access to engineering software was provided through CMC Microsystems. The authors employed the cleanroom facilities at the School of Engineering Sciences and 4DLabs at Simon Fraser University as well as Lurie Nanofabrication Facility at the University of Michigan to manufacture the devices. The authors also acknowledge the support received from National Instruments through NI Academic Research Grant Program.

REFERENCES

[1] American Standards Association, *American standard acoustical terminology*. [New York], 1951.
[2] G. C. Carter, *Coherence and time delay estimation: an applied tutorial for research, development, test, and evaluation engineers*. IEEE Press, 1993.
[3] T. B. Gabrielson, D. L. Gardner, and S. L. Garrett, "A simple neutrally buoyant sensor for direct measurement of particle velocity and intensity in water," *J. Acoust. Soc. Am.*, vol. 97, no. 4, pp. 2227–2237, Apr. 1995.
[4] A. Barbagelata, P. Guerrini, and L. Troiano, "Thirty Years of Towed Arrays at NURC," *Oceanography*, vol. 21, no. 2, pp. 24–33, Jun. 2008.
[5] C. B. Leslie, J. M. Kendall, and J. L. Jones, "Hydrophone for Measuring Particle Velocity: The Journal of the Acoustical Society of America: Vol 28, No 4," *J. Acoust. Soc. Am.*, vol. 28, 1956.
[6] G. M. Wenz, "Acoustic Ambient Noise in the Ocean: Spectra and Sources," *J. Acoust. Soc. Am.*, vol. 34, no. 12, pp. 1936–1956, Dec. 1962.
[7] H. K. Rockstad, T. W. Kenny, P. J. Kelly, T. B. Gabrielson, M. J. Berliner, and J. F. Lindberg, "A microfabricated electron-tunneling accelerometer as a directional underwater acoustic sensor," *AIP Conf. Proc.*, vol. 368, no. 1, pp. 57–68, Apr. 1996.
[8] R. Abdolvand, B. V. Amini, and F. Ayazi, "Sub-Micro-Gravity In-Plane Accelerometers With Reduced Capacitive Gaps and Extra Seismic Mass," *J. Microelectromechanical Syst.*, vol. 16, no. 5, pp. 1036–1043, Oct. 2007.
[9] R. Gholamzadeh, K. Jafari, and M. Gharooni, "Design, simulation and fabrication of a MEMS accelerometer by using sequential and pulsed-mode DRIE processes," *J. Micromechanics Microengineering*, vol. 27, no. 1, p. 015022, 2017.
[10] C.-H. Liu and T. W. Kenny, "A high-precision, wide-bandwidth micromachined tunneling accelerometer," *J. Microelectromechanical Syst.*, vol. 10, no. 3, pp. 425–433, Sep. 2001.
[11] J. Laine and D. Mougenot, "A high-sensitivity MEMS-based accelerometer," *Lead. Edge*, vol. 33, no. 11, pp. 1234–1242, Nov. 2014.
[12] "DSU1-508," 2017. [Online]. Available: http://www.sercel.com/products/Pages/DSU1-508.aspx. [Accessed: 28-Apr-2017].
[13] J. Gannon, H. Pham, and K. Speller, "A Robust Low Noise MEMS Servo Accelerometer." Technical Paper of the Applied MEMS Inc., 2001.
[14] "Colibrys - MEMS Accelerometers," *Colibrys – MEMS Accelerometers*. [Online]. Available: http://www.colibrys.com/. [Accessed: 28-Apr-2017].
[15] D. J. Milligan, B. D. Homeijer, and R. G. Walmsley, "An ultra-low noise MEMS accelerometer for seismic imaging," in *2011 IEEE SENSORS Proceedings*, 2011, pp. 1281–1284.
[16] F. Guzmán Cervantes, L. Kumanchik, J. Pratt, and J. M. Taylor, "High sensitivity optomechanical reference accelerometer over 10 kHz," *Appl. Phys. Lett.*, vol. 104, no. 22, p. 221111, Jun. 2014.
[17] H. Xu, X. Liu, and L. Yin, "A Closed-Loop Interface for a High-Q Micromechanical Capacitive Accelerometer With 200 ng/ Hz Input Noise Density," *IEEE J. Solid-State Circuits*, vol. 50, no. 9, pp. 2101–2112, Sep. 2015.
[18] B. V. Amini, R. Abdolvand, and F. Ayazi, "A 4.5-mW Closed-Loop Micro-Gravity CMOS SOI Accelerometer," *IEEE J. Solid-State Circuits*, vol. 41, no. 12, pp. 2983–2991, Dec. 2006.
[19] M. Yucetas, M. Pulkkinen, A. Kalanti, J. Salomaa, L. Aaltonen, and K. Halonen, "A High-Resolution Accelerometer With Electrostatic Damping and Improved Supply Sensitivity," *IEEE J. Solid-State Circuits*, vol. 47, no. 7, pp. 1721–1730, Jul. 2012.
[20] H. Kulah, J. Chae, N. Yazdi, and K. Najafi, "Noise analysis and characterization of a sigma-delta capacitive microaccelerometer," *IEEE J. Solid-State Circuits*, vol. 41, no. 2, pp. 352–361, Feb. 2006.
[21] H. Goldberg, "An Extremely Low-Noise MST Accelerometer Using Custom ASIC Circuitry," in *Proceedings of the Sensors Expo.*, 2000, pp. 479–482.
[22] L. Aaltonen and K. Halonen, "Continuous-time interface for a micromachined capacitive accelerometer with NEA of 4 g and bandwidth of 300 Hz," *Sens. Actuators Phys.*, vol. 154, no. 1, pp. 46–56, Aug. 2009.
[23] P. Ullah, V. Ragot, P. Zwahlen, and F. Rudolf, "A new high performance sigma-delta MEMS accelerometer for inertial navigation," in *2015 DGON Inertial Sensors and Systems Symposium (ISS)*, 2015, pp. 1–13.
[24] Z. Ye, H. Yang, T. Yin, G. Huang, and F. Liu, "High-Performance Closed-Loop Interface Circuit for High-Q Capacitive Microaccelerometers," *IEEE Sens. J.*, vol. 13, no. 5, pp. 1425–1433, May 2013.
[25] Q. Hu, C. Gao, Y. Hao, Y. Zhang, and G. Yang, "Low cross-axis sensitivity micro-gravity microelectromechanical system sandwich capacitance accelerometer," *IET Micro Nano Lett.*, vol. 6, no. 7, pp. 510–514, Jul. 2011.
[26] J. Xie, M. Song, and W. Yuan, "A high sensitivity micromachined accelerometer with an enhanced inertial mass SOI MEMS process," in *The 8th Annual IEEE International Conference on Nano/Micro Engineered and Molecular Systems*, 2013, pp. 336–339.
[27] J. Bernstein, R. Miller, W. Kelley, and P. Ward, "Low-noise MEMS vibration sensor for geophysical applications," *J. Microelectromechanical Syst.*, vol. 8, no. 4, pp. 433–438, Dec. 1999.

Copyright (c) 2017 IEEE. Personal use is permitted. For any other purposes, permission must be obtained from the IEEE by emailing pubs-permissions@ieee.org.

This is the author's version of an article that has been published in this journal. Changes were made to this version by the publisher prior to publication.
The final version of record is available at http://dx.doi.org/10.1109/JSEN.2017.2774705

[28] F. Edalatfar, S. Azimi, A. Q. A. Qureshi, B. Yaghootkar, and B. Bahreyni, "Wideband, low-noise accelerometer with open loop dynamic range of better than 135dB," in *2017 19th International Conference on Solid-State Sensors, Actuators and Microsystems (TRANSDUCERS)*, 2017, pp. 1187–1190.
[29] T. B. Gabrielson, "Mechanical-thermal noise in micromachined acoustic and vibration sensors," IEEE Trans. Electron Devices, vol. 40, no. 5, pp. 903–909, May 1993.
[30] F. Fukuyo, K. Fukumitsu, and N. Uchiyama, "Stealth Dicing Technology and Applications," presented at the 6th Int. Symp. Laser Precision Microfabrication, 2005.
[31] S. Moghaddam, "Noise Measurement in Microsensor Applications," MASc Thesis, School of Mechatronic Systems Engineering, Simon Fraser University, Surrey, BC, Canada, 2016.

Copyright (c) 2017 IEEE. Personal use is permitted. For any other purposes, permission must be obtained from the IEEE by emailing pubs-permissions@ieee.org.